Compton Scattering (^{137}Cs on BGO-crystal) and Attenuation Coefficients for ^{137}Cs

Josefine Bjørndal Robl, Lukas Martin Wick, Malthe Fiil Andersen, and Thomas Hansen

Department of Physics and Astronomy, Aarhus University

Course: Experimental Physics 3

Experimental exercise 3

(Dated: September 25, 2019)

Using a ^{137}Cs source this paper aims to determine the angular distribution of Compton scattering of photons on a BGO-crystal, along with the attenuation coefficients of aluminum, copper, lead and brass. By measuring the photons detected in an inner BGO detector and an outer NaI detector with respect to the scattering angle, and filtering the data due to time and energy constrains, Compton scattering of a photon on a BGO-crystal is measured. For angles from and above $40°$ the measurements are consistent with the theoretical curve (figure 2), but for smaller scattering angles the non-linearity of this curve influence the measurements due to the NaI detector measuring a small range of angles due to its extend.

Using a ^{137}Cs source the attenuation coefficients were measured by positioning the plates between the source and detector (with room to spare) and one by one removing a plate and measuring the number of counts in $2.5\,\mathrm{min}$. Fitting the peak to a Gaussian the following attenuation coefficient were achieved:

$$\mu_{Al} = 0.204(7)\,\mathrm{cm}^{-1}, \quad \mu_{Brass} = 0.67(2)\,\mathrm{cm}^{-1}, \quad \mu_{Pb} = 1.12(2)\,\mathrm{cm}^{-1}, \quad \text{and} \quad \mu_{Cu} = 0.65(2)\,\mathrm{cm}^{-1},$$

all being close (μ_{Al} and μ_{Cu} within their respective uncertainty) to the theoretical values, and μ_{Brass} being close to μ_{Cu} as expected do to its presumed composition of mainly copper. Due to the lead plates being allowed a small angle to vertical to stay upright and the slightly bending of the plates, the photons have had to travel a longer distance than assumed, hence explaining the μ_{Pb} of lead to be less than expected.

I. INTRODUCTION

The quasielastic process of Compton scattering is a well know phenomenon of scattering photons by electrons, both bound and free with the latter being more well studied than the former [1]. Compton scattering is studied for its broad spectrum of applications in various scientific fields such as physics, chemistry, and biology [2], an example being in radiobiology to differentiate between normal and diseased breast tissue in patients suspected of having cancer [3], since Compton scattering is one of the most probable interaction of gamma rays and high energy X-rays with atoms in living beings. Hence the importance of studying the scattering of photons by bound electrons is crucial for our continued progress in the scientific fields. There-fore this paper aims to determine the angular distribution of Compton scattered photons from ^{137}Cs on a BGO-crystal, thus relating the energy of Compton scattered photons to their scattering angle. Another purpose of this paper is to study the attenuation coefficients of various materials including aluminum and brass also using a ^{137}Cs source, due to the attenuation coefficients crucial use in radiation shielding.

II. THEORY

A. Attenuation Coefficients

When gamma radiation go through a material three primary effects will decrease its intensity: photo elec-

tric absorption, Compton scattering, and pair production. For the ^{137}Cs source used in this project the co This leads to a loss of total radiation.Compton scattering is the dormant effect [4]. It is expected that the change of intensity through a piece of material of thickness dt is proportional to some material specific constant, the intensity itself and the thickness itself:

$$\frac{\mathrm{d}I}{I} = -\mu \mathrm{d}t, \tag{1}$$

where μ is the proportionality coefficient also known as the attenuation coefficient.

This leads to the following formula:

$$I(t) = I_0 \exp\left(-\mu t\right) \tag{2}$$

I_0 denotes the initial intensity. [4]

B. Compton Scattering

Compton-scattering occurs when a photon hits an electron, which is either loosely bound or free, and then delivers some, but not all, of its energy to the electron and is thus sent on a different trajectory.

Then by requiring conservation of 4-momenta an equation of the photon energy after the scattering can be derived:

$$E_{\gamma'} = \frac{E_\gamma}{1 + (E_\gamma/mc^2)\left(1 - \cos\theta\right)}, \tag{3}$$

where $E_{\gamma'}$ is the energy of the photon after the scattering, and E_γ is the energy of the photon prior to scattering. θ is the scattering angle and m is the mass of the electron.

Using quantum-mechanics the *Klein-Nishina formula* can be derived:

$$\frac{\mathrm{d}\sigma}{\mathrm{d}\Omega} = r_0^2 \left[\frac{1}{1 + \alpha\left(1 - \cos\theta\right)}\right]^3 \left[\frac{1 + \cos\theta}{2}\right]$$
$$\left[1 + \frac{\alpha^2\left(1 - \cos\theta\right)^2}{\left(1 + \cos^2\theta\right)\left(1 + \alpha\left(1 - \cos\theta\right)\right)}\right], \tag{4}$$

where σ is the cross section, Ω is the solid angel, and α is $E\gamma/(mc^2)$. [4]
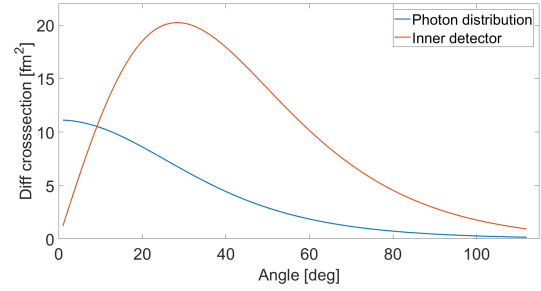

Figure 1: Graph of the differential cross section by the angle (θ) in degrees, for the Compton-scattering with ^{137}Cs source.
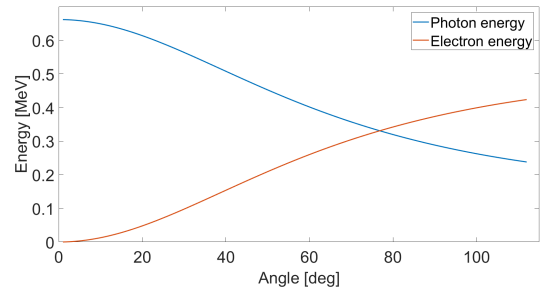

Figure 2: Plot of the energy of the scattered photon by the angle of scattering (θ).

In this experiment a Cesium 137 source was used, which gives $E_\gamma = 661.64\,\mathrm{keV}$ [5]. The rest energy of the electron is $510.999\,\mathrm{keV}$ [6] giving $\alpha = 1.2948$.

This results in a differential cross section given on figure 1, and an energy given by an angle to the original photon trajectory see figure 2.

The inner detector, measuring the energy of electrons that the photons have scattered on, have a somewhat different energy. The energy is simply given by the change in energy of the photon upon scattering, see figure 2. The probability distribution is given by the same distribution as for the photon, however, the distribution seen needs to be integrated over all the positions at which the angle to the beam is θ.

In order to compare it with the data we plot the distribution as a function of energy (see figure 3).

C. Detectors

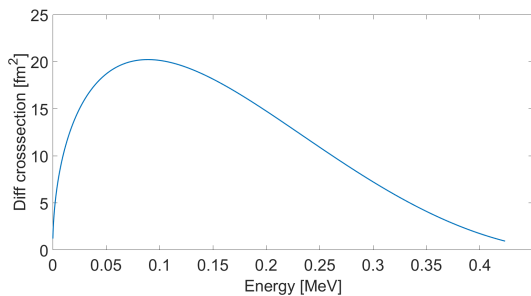The detectors used in this project are scintillator detectors.

Figure 3: Plot of the differential cross section of Compton-scattering integrated over the azimuth angle (in relation to the beam) at for different fixed energy.

Scintillator detectors work through the following mechanism:

1. Incident radiation hits the scintillating material, resulting in the atoms being raised to excited states. This leads to the material releasing photons; the material is fluorescing.

2. The emitted photons hit a photosensitive surface releasing at maximum one electron per incident photon.

3. Those electrons are then multiplied in a photo multiplier tube (PM). This is done using a series of plates called dynodes with a potential of about 100V between them. This is more than enough to cause electrons to be released from the dynodes when they are hit by an electron, causing a multiplication of intensity of 30-50 times.

The most commonly used inorganic material is NaI, as used in the outer detector[1]. As NaI is an insulator, when an electron is hit by radiation it (generally) jumps from the valence band to the conduction band - a gap of about 4eV, after which the electrons jump back and emit a photon, which may hit the photosensitive surface later.

Often impurities is introduced to the crystal, for example to a NaI detector thalium (Tl) is often used. Introducing thalium moves the wavelength of maximum emission from about 303 nm to 410 nm, increasing the efficiency of the detector as most photosensitive plates are most sensitive in the visible spectrum. It also manages to decrease the likelihood of self-absorption of the

———

[1]See figure 4 and figure 6

emitted photons, thus in total drastically increasing the efficiency of the detector. [4]

III. SETUP AND PROCEDURE

A. General setup

The detector used for the electrons is a BGO detector. It has worse timing capabilities than the NaI(Tl) detector and about 2 times worse resolution. The only real advantage of the BGO detector is its superior stopping power, giving a higher frequency of scattering, making it a good choice for the inner detector. [7] The detector used for the scattered photons is an NaI(Tl)-detector.

B. Calibration

Both detectors needed their own calibration from channel number to energy. For the NaI(Tl) detector the isotope ^{226}Ra (6 peaks) were used. The BGO-detector was positioned such that only the ^{137}Cs peak could be obtained.Therefore the channel-number-/energy-graph was forced to go through $(0, 0)$ to obtain a calibration. The NaI(Tl) detector was placed on a table shielded from surrounding radioactive sources by lead bricks. When the setup was ready to measure, the relevant source were retrieved and balanced on the table against the end of the detector. A measurement was taken using Mc^{2}Analyzer in listmode.

C. Attenuation Coefficients

A picture of the setup is shown in figure 4. A ^{137}Cs source is used. The radiation is collimated by a lead block in which a hole has been drilled. Just outside the hole the absorbing materials are placed. The placement of the detector should be held constant, it should also be some distance from the material. The distance from the material is due to the background radiation. Changing the shielding of the detector would change the background, which would worsen the measurements. If the detector is placed in contact with the shielding material, that would happen. The collimation is never perfect and as such the degree to which the beam can increase in size was estimated by measuring the depth and diameter of the
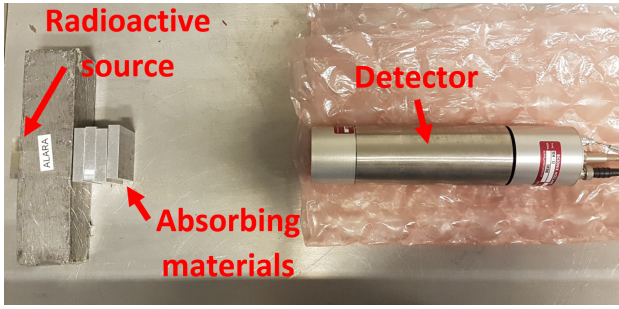
Figure 4: The setup for measuring attenuation coefficient. A radioactive source ^{137}Cs is placed behind a lead bar with a cylindrical whole of $4.5(2)$ mm in diameter to obtain an approximately collimated beam.

Figure 5: The collimating lead block and the radioactive source.

hole using a caliper, see figure 5. The diameter of the NaI(Tl) crystal was taken from [8]. This gave a maximum distance the detector could be placed at of about 50 cm. The distance needed to be between the two things and $25.3(5)$ cm was chosen.

The measurements were taken in 2.5 minutes, real time (including the dead time of the detectors). The materials thickness were measured again using calipers. The materials were stacked, the full thickness were measured, one slate was removed, the thickness was remeasured and repeat.

The thickness of lead was not measured that way as they were wavy, and thus couldn't be measured in that way. They were measured individually. This increases uncertainties on the thickness.

The measurements stared the maximum amount of material, and went down, one slate at a time.

D. Compton Scattering

The NaI detector were mounted in the movable tube leading the scattered photons from the BGO detector to the NaI(Tl) detector, see figure 6, and screwed into place using small plastic screws on the side of the tube. The Compton scattering of photons from the ^{137}Cs source on the BGO detector were measured every ten degree from 20° to 110° alongside 25° and 65°, since these are angles, where the Compton scattering would change a lot, see figure 2. Up to and including the angle 40°, the measurements were taken in 10 min real time (thus including detector dead time), while the measurements from and including 50° were taken in 15 min, since the larger the angle the lesser the counts. The time difference is taken into account in the data
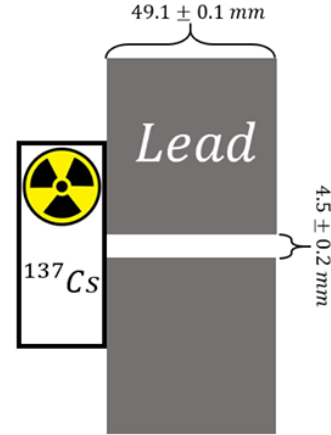

Figure 6: The setup of the Compton scattering measurements. A ^{137}Cs source enclosed by lead blocks (top left) send a beam towards a BGO detector (top middle) at where the photons Compton scattered, and the resulting photons were lead through a movable tube to the NaI(Tl) detector (bottom right).

analysis.

For the Compton scattering measurements the data collected were already lightly sorted in the sense that only the measurements that are measured in both detectors within a time limit of 2.55 µs are counted, using the Coincidence in Mc^{2}Analyzer.

IV. RESULTS

A. Calibration

The calibration seems to drift between different times of measurement (probably due to technical issues leading to slightly different configurations). Therefore only the calibration measurement on ^{226}Ra at the day of the Compton measurements are taken into account[2] (The attenuation measurements does not need precise calibration).

A source were placed in front of the NaI, and a measurement was taken over a sufficient time giving a spectrum as can be seen in figure 7. The spectrum is a histogram counting all measurements n in each channel, and setting the uncertainty in for each channel the square root of the number of counts $\sigma_{\text{counts}} = \sqrt{n}$.

The prominent peaks where fitted using a Gaussian (of the form in equation (6)), to find the center. These fits can be seen in figure 7, together with the established value for each peak, from [9]. All of these fits had reasonable MSE (Mean Square Error defined as Chi squared over degrees of freedom of the fit) values of around 1 which given we are only interested in their top points and not their general distribution is fully acceptable. The uncertainty in the center of the peak was found from the fit.

Now the channel number (denoted Ch) can be plotted against energy and a straight line can be fitted through the points as in figure 8. As the uncertainties are very low a plot of the residuals from the fit is plotted in figure 9 together with the confidence intervals. The results of the fit is:

$$E = 1.269(7)\,\text{keV} \cdot Ch + 13(2)\,\text{keV}. \quad (5)$$

The MSE of this fit was 7.1.

For the BGO detector only the ^{137}Cs source was used for calibration (with one peak at $0.661\,64$ MeV [5]). As before the peak in the spectrum was fitted as can be seen in figure 10. The peak was found at channel 554.3(5) Assuming Channel 0 correspond to $E = 0$ this gives $E = 1.194(1)\,\text{keV} \cdot Ch$

---

[2]The ^{226}Ra source accounted for most of the points, so the others weren't retaken.

B. Attenuation

The goal of this section is to fit μ in equation (2). For each measurement a spectrum is measured. In this spectrum a Gaussian of the form

$$n = \beta_1 \exp\left(-\left(\frac{Ch - \beta_2}{2\beta_3}\right)^2\right) + \beta_4 Ch + \beta_5, \quad (6)$$

is fitted, where n is the number of counts in the channel Ch and $\beta_4 Ch + \beta_5$ is an approximation of the form of the background. A plot of this fit on one measurement, with the background marked, is shown in figure 11.

The total integral over the Gaussian part of equation (2) is approximately the same as the number of counts for that peak N which is proportional to the intensity of the beam by $N = CI$ for some constant C. N can be found by the integral:

$$N = \int_{-\infty}^{\infty} \beta_1 \exp\left(-\left(\frac{Ch - \beta_2}{2\beta_3}\right)^2\right) d(Ch) \quad (7)$$

$$= 2\sqrt{\pi}\beta_1\beta_3 \quad (8)$$

The uncertanty of N is found by propagation of error for the fitted uncertainties in the variables β_1, β_3 and recursively for the uncertainty in the thickness of the plate of about $\sigma_t = 0.02$ mm. To fit μ the data is fitted to the expression:

$$N = \beta e^{-\mu t},$$

with fitting parameters β and μ. Here β will be $C \cdot I_0$ where C is some constant. These fits for each material can be seen in figure 12 (with logarithmic y-axis) and the values can be seen in table I. The expected values of μ has been obtained by fitting an exponential functions to four values of $\mu(E)$ from [10] around the energy $E = 661.64$ KeV. The attenuation coefficient of brass depends on the precise alloy used which were not known.

Table I: Found and expected attenuation constants for the different materials, with quality of fit.

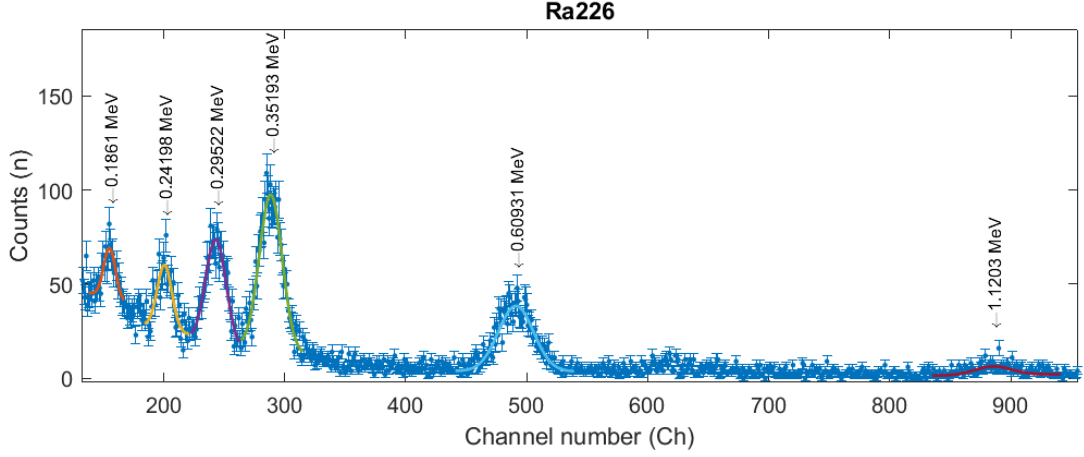| Material	Found μ [cm^{-1}]	Expected μ [cm^{-1}]	P-value of fit
Al	0.204(7)	0.2017(4)	0.477
Brass	0.67(2)	Unknown	0.798
Pb	1.12(2)	1.25(2)	0.969
Cu	0.65(2)	0.651(3)	0.973

Figure 7: Spectrum for a measurement of Ra-226 for 5 minutes. Prominant peaks fitted, and assigned established values for energy (from [9]).)
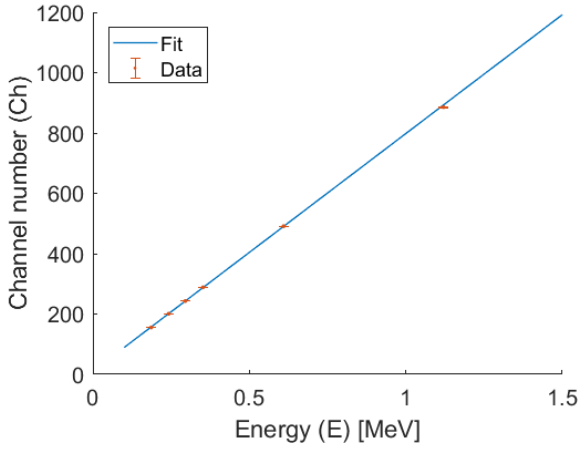

Figure 8: Calibration fit. Found channel numbers of peaks vs their found energy and the line fits to the data. MSE of fit: 7.1

Figure 9: Residual plot of calibration fit in figure 8

C. Compton scattering

When measuring Compton scattering using the procedure described in section III D, both the inner and outer detector will see not only Compton scattered particles, but also background radiation. This is most relevant for the outer detector, since the overall intensity at that position is way lower than for the inner detector. The inner detector, however, will detect not only the Compton scattered particles for every spacial angle, but also total absorption of the
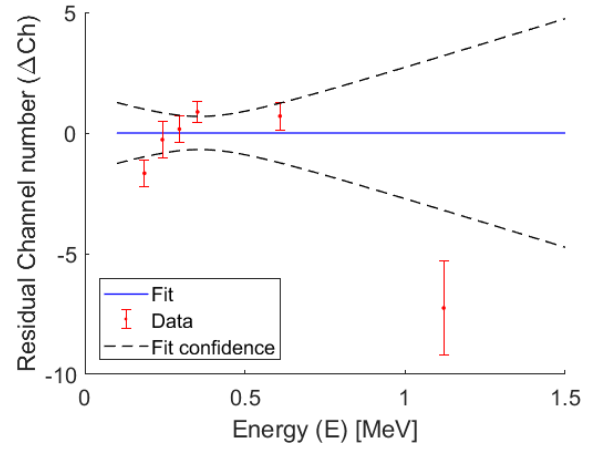
radiation (and background). The detections of totally absorbed events result in a sharp peak around the cesium-137 radiation energy. However, when a Compton-scattering event occurs only some of the energy will be released in the inner detector, and thus all Compton-scattered events result in a broader spectrum energetically below the total absorption peak. The theoretical shape of this peak can be seen in figure 3. An example of the raw data of the inner detector can be seen in figure 13.

In order to count the number of Compton-scattering events at a given angle, a method to filter all the irrelevant detections away is needed. This can be done
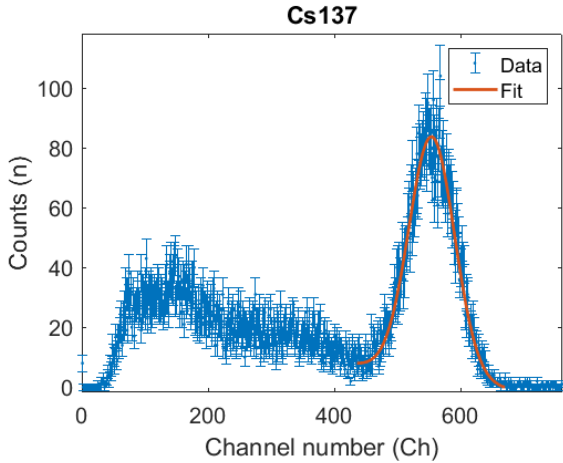
Figure 10: Spectrum for a measurement of Cs-137, with fitted peak.
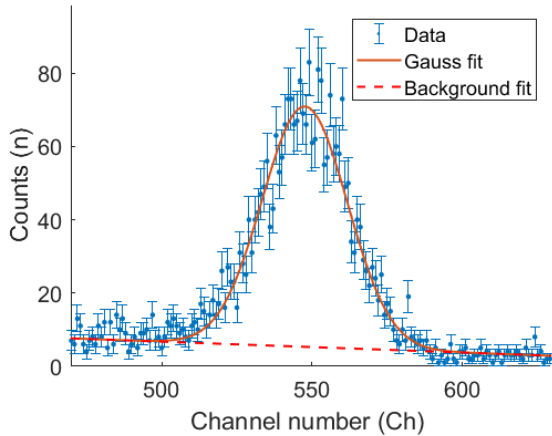

Figure 11: Gauss fit of Cs-137 peak with 1 plate of aluminum, with linearly fitted background marked.

by demanding, that a detection of a scattered particle in *both* the inner and outer detector must correlate in time and energy.

The event in the inner detector must, of course, occur before the related event in the outer detector. On the other hand, the time difference cannot be too large either. The exact time tolerance depends on the equipment and setup and must be measured. The first step is then to filter all the data in the two detectors using a too large initial time tolerance. By plotting the resulting number of events as a function of time difference between the two detectors, we then expect

to see a peak around the correct time tolerance (since background noise assumingly distributes evenly, but the scattering data only occurs at the right time tolerance). See figure 14. Using the information a better guess for the time tolerance can be made.

We then filter the data again using a rough guess for the energy *spread* (the correct energy is already known either by the high energy peak in the inner detector or by general knowledge about the cesium source). This data is plotted in figure 15. Several peaks can be spotted, but only the peak around the cesium energy (about 661keV [5]) is relevant. The other peaks are a consequence of the relatively huge amount of noise compared to the intensity of the Compton-events. Some of the noise events simply happen to lie within the time tolerance (but not within the time tolerance *and* the energy tolerance at the same time, if the energy tolerance is taken to only span the peak around energy 661keV).

Using the correct tolerances, the original data can now be filtered, and the number of accepted scattering events counted. The result as a function of the scattering angle can be seen in figure 16, where it is fitted to the expression in equation (4) multiplied by a fitting constant β_1 plus another fitting constant β_2.

V. DISCUSSION

A. Calibration

The calibration function can be seen in equation (5) In general the calibrations seem to bee somewhat consistent with a small drift over time, making calibrations for each measurement day preferable, which was done. The relatively large MSE for the fit of calibration coefficients (figure 8) indicates slightly underestimated uncertainties in the centers of the peaks, which might in turn results in underestimated uncertainties in calibration coefficients. However at this level it is not the largest concern as other sources of uncertainty far outweigh these effects in the sorting of the Compton scattering experiment, and the data points do not differ a lot from a straight line.

B. Attenuation

The fits to the peaks (under which the number of counts was calculated) seem reasonable (figure 11),
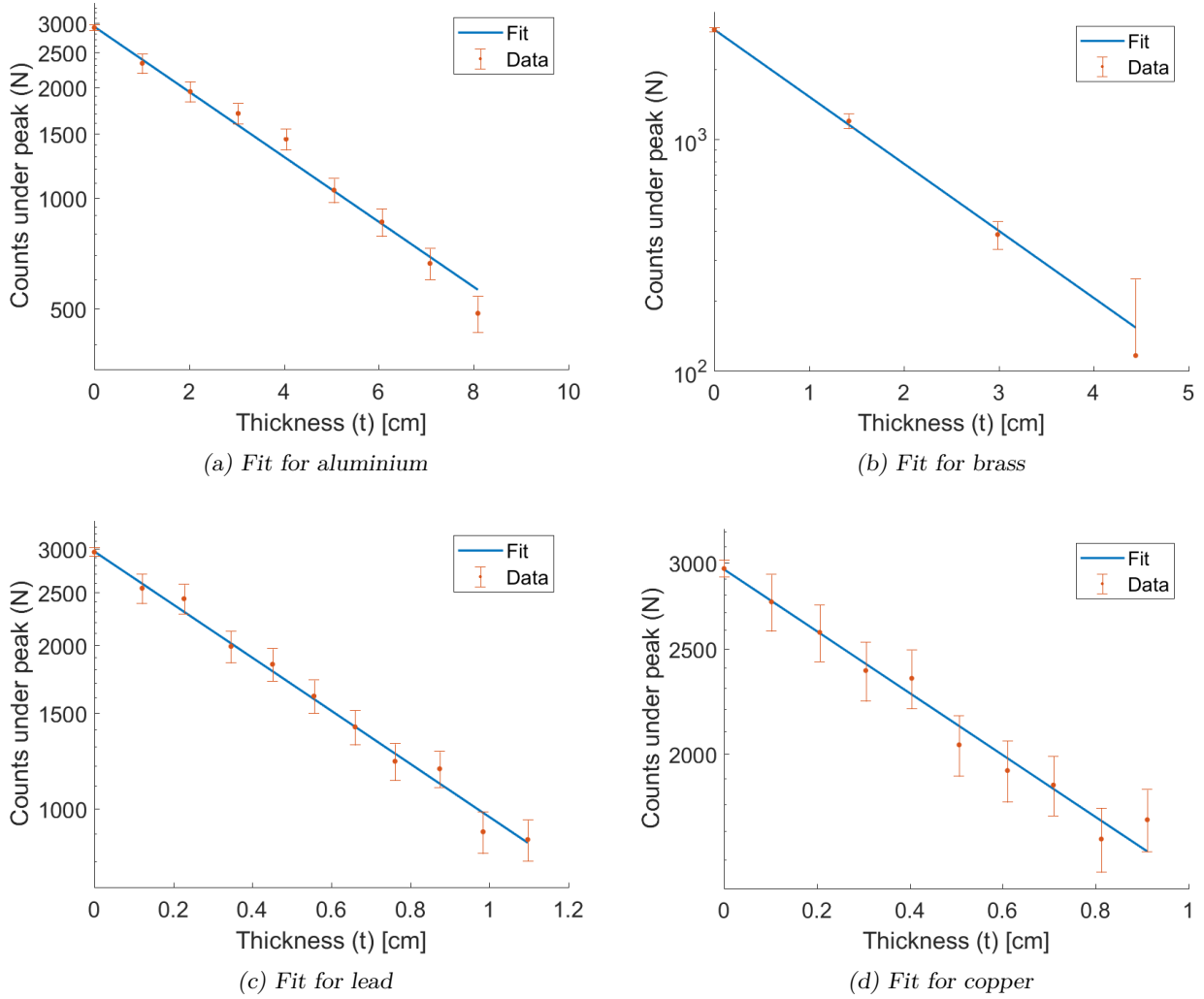
Figure 12: Exponential fits of the attenuation coefficient for the four materials. N.b. the logarithmic y axis.

as well as the fits to the attenuation coefficients (figure 12) which all has acceptable P-values. The attenuation constants (table I) seem to be quite accurate for Cu and Al, with the found and expected values lies well within the uncertainty. (Maybe indicating a slightly over calculated uncertainty). For lead it seems some systematic error has an rather large effect. This could be caused by the lead being an alloy, or a difference between the actually traveled length in the material and the measured length. If the actual length is lager than the measured, the found μ should be less than expected, which is what was found. This could be due to the plates being bended, at an angle

or the measurements of the material e.g. if the plates were compressed under the Callipers. However with the quite accurate findings for Cu and Al it is reasonable to believe that the found coefficient for Brass is quite accurate and it could probably be used to find the composition of the brass. It is also worth noting that it lies close to the value of Cu as expected, as brass consists largely of Cu.
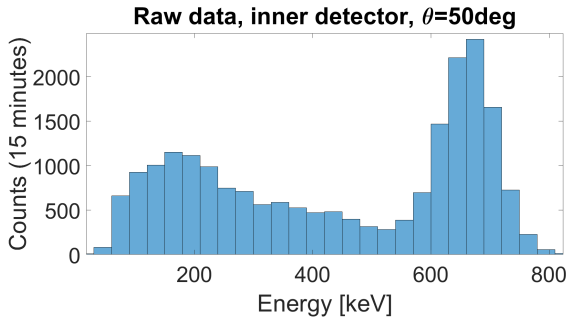
Figure 13: The raw data from the inner detector at angle θ = 50deg. The left peak resembles that of the theory in figure 3. The right peak is complete absorption of radiation at the correct energy of approximately 660keV.
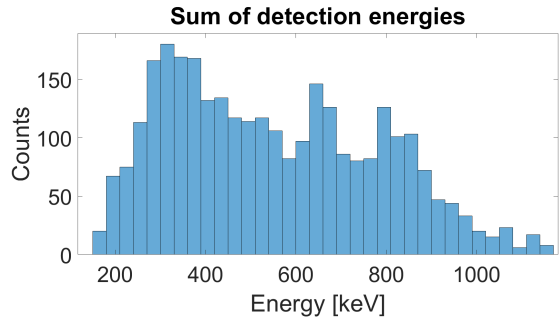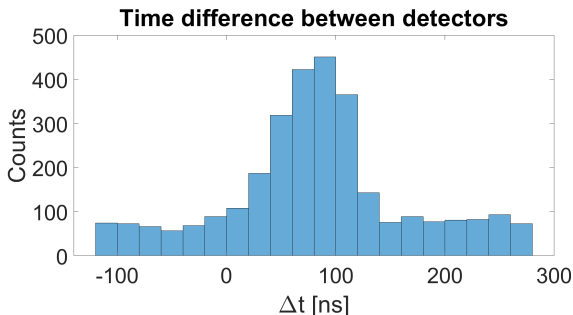

Figure 14: A plot of the number of accepted counts for given time intervals between events at the inner and outer detector. A clear peak appears as expected.

C. Compton scattering

The pattern of Compton-scattering on the inner detector follows the expectations from theory (figure 13). Both the scattering "peak" and the absorption peak is clearly visible indicating that Compton-scattering is actually happening.

Another strong indication is the peak in the time difference plot (figure 14). Had Compton-scattering not occurred the outer detector would not detect correlated events a fixed time *after* events in the inner detector. The exact size of the time difference depends on the apparatus.

A problem starts to arise when energy is considered too. The amount of noise compared to the events of interest is considerable as can be seen in figure 15. To deal with this, a very tight energy tolerance of ±50keV was chosen. This cuts off most of the noise. However, we also loose some of the actual Compton-

Figure 15: A plot of the counts versus the sum of energies in the two detectors (using events only within the initial time tolerance).

events in doing so. Assuming the relative amount of lost Compton-events is a constant, this should not affect the shape of the final graph (figure 16).

Considering the uncertainties, the theoretical prediction does not correspond well with the data. We expect two effects to be the reason for this.

Firstly, the outer detector was able to detect scatter-events in an extended angle of a few degrees. If the slope of scatter-intensity versus angle is constant, this will have no effect, since the detections will even out. But if a non-zero second derivative, this becomes important. For positive second derivatives, there will be an overestimation of events, while the opposite happens for negative second derivatives. As can be seen in the final data, the overestimation occurs when the second derivative is greatest.

Secondly, low scattering angles result in low energies (On the inner detector), which are harder to detect. On top of that, more background radiation will hit the outer detector on low angles. Most importantly, it becomes harder to sort the actual scattering events and the noise. Ultimately, this results in underestimations of the data. This effect is clearest in the data plotted in red in figure 16. When using lifetime measurements low angles might also have a larger percentage "downtime" resulting in less obtaiend data.

VI. CONCLUSION

The attenuation coefficients in the experiments were found to be $\mu_{Al} = 0.204(7) \, \text{cm}^{-1}$, $\mu_{Brass} = 0.67(2) \, \text{cm}^{-1}$, $\mu_{Pb} = 1.12(2) \, \text{cm}^{-1}$, and $\mu_{Cu} = 0.65(2) \, \text{cm}^{-1}$. The experimental attenuation coefficients for aluminum and copper are consistent
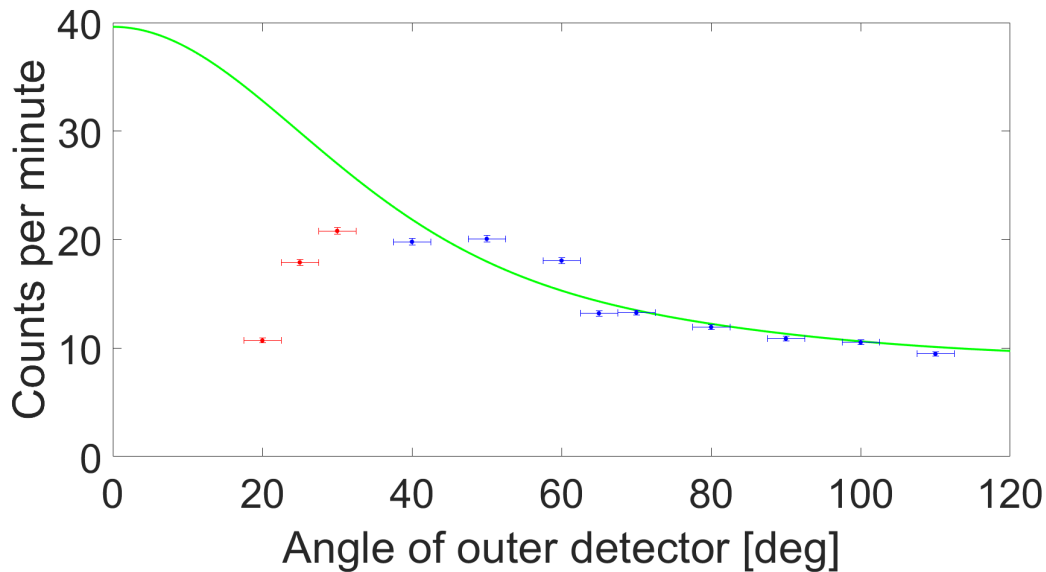
Figure 16: The detected Compton-scattered events per minute as a function of the scattering angle. The result is compared to the green theoretical plot on top. The low-angle measurements drop off considerably. Uncertainties are estimated by $\sqrt{N}/t$ on the second axis, where t is the time of measurement, and on the first axis by geometrical features of the setup.

with their theoretical attenuation coefficients within the uncertainty, $\mu_{Al,theory} = 0.2017(4)\,\mathrm{cm}^{-1}$ and $\mu_{Cu,theory} = 0.651(3)\,\mathrm{cm}^{-1}$. Due to us not being aware of the composition of brass other than it is an alloy composed mostly of copper, its attenuation coefficient is expected to be near the attenuation coefficient of copper, which is also seen. The experimental attenuation coefficient of lead was a bit of from the theoretical attenuation coefficient $\mu_{Pb,theory} = 1.25(2)\,\mathrm{cm}^{-1}$ possibly due to two factors; the lead plates were allowed a small angle to vertical since they otherwise would not be able to stay standing between the ^{137}Cs and the NaI detector, and the plates used being slightly bended, both resulting in a longer travel distance for the gamma rays than the expected.

For the Compton scattering the obtained data are consistent with the the theoretical curve presented in figure 2 for the angles of 40° and above, while the data for 20°, 25° and 30° deviates quite a lot from the theoretical curve, possible due to the measured electron energy on the BGO detector being lowest for the low scattering angles and the detectors finding this hard to detect especially when considering the larger background radiation (in proportion to the detections). Another factor for the deviation is the NaI detector being able to detect scatter events in an extended angle of a few degrees, which for small scattering angles will have a larger impact, since the theoretical curve here is non-linear, thus having a non-zero second derivative, and this being positive will result in an overestimation of events explaining the data beneath the theoretical curve.

[1] I. A. Gnilozub, A. Galstyan, Y. V. Popov, and I. P. Volobuev, "Coherent Compton scattering from hydrogen and helium atoms," *J. Phys. B: At. Mol. Opt. Phys.*, vol. 52, p. 035204, September 2018. arXiv: 1809.08815.

[2] L. Guang, Z. Shang-qi, H. Zhong, and C. Shuang-kou,

"Applications of Compton scattering," vol. 5, p. 7, December 2006.

[3] E. A. Ryan, M. J. Farquharson, and D. M. Flinton, "The use of Compton scattering to differentiate between classifications of normal and diseased breast tissue," *Phys. Med. Biol.*, vol. 50, pp. 3337–3348, July

2005.

[4] K. S. Krane and D. Halliday, *Introductory nuclear physics*. New York: Wiley, 1987. Chapter 7 *Detecting nuclear radiations*.

[5] P. Siegel, "Gamma Energy (KeV)." URL: `https://www.cpp.edu/~pbsiegel/bio431/genergies.html`. Accessed on September 11th 2019.

[6] The National Institute of Standards and Technology (NIST), "CODATA Value: electron mass energy equivalent in MeV." URL: `https://physics.nist.gov/cgi-bin/cuu/Value?mec2mev`, May 2019. Accessed on September 19th 2019.

[7] Saint-Gobain Ceramics & Plastics, Inc, "Compton Suppressor Shields NaI(Tl) versus BGO," August 2018.

[8] SCIONIX, *VS-0008-55.dft.* Scionix Holland B.V., May 2019. URL: `https://blackboard.au.dk/bbcswebdav/pid-2291318-dt-content-rid-6997242_1/courses/BB-Cou-UUVA-84828/BB-Cou-UUVA-84828_ImportedContent_20190708112422/NaI.pdf`.

[9] Eckert Ziegler Nuclitec GmbH, "Recommended Nuclear Decay Data, Ra-226." URL: `https://www.ezag.com/fileadmin/ezag/user-uploads/isotopes/isotopes/Isotrak/isotrak-pdf/Decay_Schema_Data/Ra-226.pdf`. Accessed on September 21st 2019.

[10] J. H. Hubbell and S. M. Seltzer, "X-Ray Mass Attenuation Coefficients." URL: `https://www.nist.gov/pml/x-ray-mass-attenuation-coefficients`. Accessed on September 24th 2019.